Monthly Notices
of the
ROYAL ASTRONOMICAL SOCIETY

MNRAS **461,** 4260–4275 (2016)
Advance Access publication 2016 July 7

doi:10.1093/mnras/stw1627

The complex star cluster system of NGC 1316 (Fornax A)

Leandro A. Sesto,[1,2,3★] Favio R. Faifer[1,2,3★] and Juan C. Forte[3,4★]

[1]*Facultad de Cs. Astronómicas y Geofísicas, Univ. Nac. de La Plata, Paseo del bosque S/N, B1900FWA LA Plata, Argentina*
[2]*Instituto de Astrofísica de La Plata, Paseo del bosque S/N, B1900FWA LA Plata, Argentina*
[3]*Consejo Nacional de Investigaciones Científicas y Técnicas (CONICET), Rivadavia 1917, C1033AAJ Ciudad Autónoma de Buenos Aires, Argentina*
[4]*Planetario 'Galileo Galilei', Secretaría de Cultura, Av. Sarmiento S/N, 1425 Ciudad Autónoma de Buenos Aires, Argentina*

Accepted 2016 July 4. Received 2016 July 4; in original form 2015 December 4

ABSTRACT

This paper presents Gemini-*gri*′ high-quality photometry for cluster candidates in the field of NGC 1316 (Fornax A) as part of a study that also includes GMOS spectroscopy. A preliminary discussion of the photometric data indicates the presence of four stellar cluster populations with distinctive features in terms of age, chemical abundance and spatial distribution. Two of them seem to be the usually old (metal poor and metal rich) populations typically found in elliptical galaxies. In turn, an intermediate-age (5 Gyr) globular cluster population is the dominant component of the sample (as reported by previous papers). We also find a younger cluster population with a tentative age of $\approx$ 1 Gyr.

Key words: galaxies: elliptical and lenticular, cD – galaxies: haloes – galaxies: photometry – galaxies: star clusters: general.

1 INTRODUCTION

Once considered as 'simple systems', globular clusters (GCs) are steadily leaving that characterization as more complex features of their stellar populations are discovered, e.g. Carretta (2015). This situation emphasizes the problem of not only understanding their formation as individuals but also in the context of galaxy formation (e.g. Brodie et al. 2014; Harris, Harris & Hudson 2015; Kruijssen 2015, 2016).

The idea that GC systems are connected with large-scale features of galaxies has its roots in Eggen, Lynden-Bell & Sandage (1962). A recent example of this kind of analysis can be found in Forbes et al. (2016).

If GCs are in fact tracers of the dominant stellar populations formed in different events during the life of a galaxy, they should reflect some common features with field stars (e.g. in terms of ages, chemical abundances and spatial distributions).

In this frame, NGC 1316, a giant elliptical galaxy and strong radio source (Fornax A), appears as a particularly attractive object. On one side, the galaxy displays a number of morphological features that seem the fingerprints of 'merger' activity (shells, ripples, complex dust lanes) that have been studied in the optical range, for example, by Schweizer (1980, 1981). On the other, the galaxy exhibits a prominent GC system that has distinctive characteristics when compared with other bright ellipticals. The presence of 'intermediate' age clusters in this galaxy, and their importance in the context of GCs formation, was already pointed out by Goudfrooij et al. (2001a) and subsequent studies (Goudfrooij et al. 2001b, 2004; Goudfrooij 2012).

★ E-mail: sesto@fcaglp.unlp.edu.ar (LAS); favio@fcaglp.unlp.edu.ar (FRF); forte@fcaglp.unlp.edu.ar (JCF)

A key feature in this analysis is the identification of the different kind of cluster systems that co-exist in NGC 1316. For example, Goudfrooij et al. (2001b) show that the integrated brightness-colour domain occupied by the 'blue' GCs in this galaxy is very similar to that of the low metallicity and old halo clusters in the Milky Way (MW). In turn, that work also pointed out that 'intermediate' colour GCs are considerably brighter in the average, then suggesting younger ages.

Some of the features of the NGC 1316 GC system were studied by Gómez et al. (2001) on the basis of *BVI* photometry. That work derived an overall ellipticity of 0.38 with a position angle (PA) of 63 deg for the whole cluster system. Besides, their analysis of the projected areal density of the GCs as a function of galactocentric radius suggests that both the 'blue' and 'red' subpopulations share, to within the errors, very similar slopes.

A more recent attempt to disentangle the GCs populations using wide-field ($C - R$) photometry has been presented by Richtler et al. (2012b). These authors explore the possible presence of two or three cluster populations and conclude that the dominant component is as young as 2 Gyr.

In turn, Richtler et al. (2014) presented a thorough study of the kinematic behaviour of the GC system of NGC 1316 based on the radial velocities (RVs) of 177 GCs. In another work, Richtler et al. (2012a) concentrated on the so-called SH2 object, finding that it is in fact an unusual region of star formation.

A recent estimate of the distance modulus of NGC 1316 has been presented by Cantiello et al. (2013), who derive $(m - M)_0 = 31.59$ (20.8 Mpc) by means of the surface brightness fluctuations (SBF) method, that we adopt in this paper, and is somewhat smaller than that given in Goudfrooij et al. (2001a): $(m - M)_0$=31.80.

In this work, we present high-quality Gemini-*gri*′ photometry carried out on a CCD mosaic including eight different fields. This

Table 1. Summary of observations. This table lists the identification number of the fields, airmass, exposures and final seeing of the co-added images.

Galaxy	Field	Airmass			$T_{exp.}$(s)			FWHM (arcsec)		
		g'	r'	i'	g'	r'	i'	g'	r'	i'
NGC1316	1	1.112	1.112	1.140	4×300	4×150	4×150	0.90	0.83	0.80
	2	1.009	1.020	1.033	4×360	4×200	4×200	0.85	0.75	0.67
	3	1.067	1.013	1.017	4×300	4×150	4×150	0.75	0.72	0.63
	4	1.090	1.050	1.067	4×300	4×150	4×150	0.90	0.80	0.78
	5	1.180	1.024	1.035	4×360	4×150	4×150	0.75	0.75	0.83
	6	1.435	1.319	1.255	4×360	4×200	4×200	1.00	0.85	0.80
	7	1.111	1.069	1.048	4×360	4×200	4×200	0.78	0.70	0.67
	8	1.072	1.115	1.150	4×360	4×200	4×200	0.70	0.50	0.50
Standard	E2-A	1.043	1.044	1.045	1×10	1×10	1×10	–	–	–
Blank sky	–	–	–	1.153	–	–	7×300	–	–	–

material is part of a study (in progress) that also includes GMOS spectroscopy for some 35 confirmed GCs. Currently, deep GC spectroscopic data are only available for three GCs (Goudfrooij et al. 2001a).

Low photometry errors are crucial for a characterization of the different cluster populations. In turn, the use of three different filters allows us to account for field contamination and also for a comparison with simple stellar population (SSP) models in two colour diagrams.

The paper is organized as follows: the characteristics of the data handling and photometry, including an analysis of the errors and completeness, are presented in Section 2. At the same time, in this section we made the selection of unresolved sources and examined their colour–magnitude diagram. In Section 3, we analysed the distribution of the GCs on the sky as well as the colour–colour relations. An attempt to derive ages and chemical abundances using SSP models is presented in Section 4. The spatial distribution of each GC subpopulation and the behaviour of the areal density profiles is discussed in Section 5. A brief discussion of the RVs and of the GC integrated luminosity function are given in Sections 6 and 7, respectively. Finally, a summary of the main conclusions is presented in Section 8.

2 DATA HANDLING AND PHOTOMETRY

2.1 Observations and data reduction

The data set used in this work, listed in Table 1, was observed in image mode with the GMOS camera, mounted on Gemini South telescope, between 2008 September–October and 2009 August–October (Programmes GS-2008B-Q-54 and GS-2009B-Q-65, PI: J.C. Forte).

Four images per field with a binning of 2×2 were taken through SDSS g', r' and i' filters (Fukugita, Ichikawa & Gunn 1996). These single exposures were obtained following a dithering pattern between them to facilitate cosmic ray cleaning and to fill the gaps between the CCD chips. The distribution of the eight observed GMOS fields forms a mosaic as it is shown in Fig. 1.

The reduction process includes the correction for instrumentals effects, the creation of mosaics and the combination of different exposures for each filter. With that goal, the raw images were processed using the Gemini GMOS package within IRAF[1] (e.g.

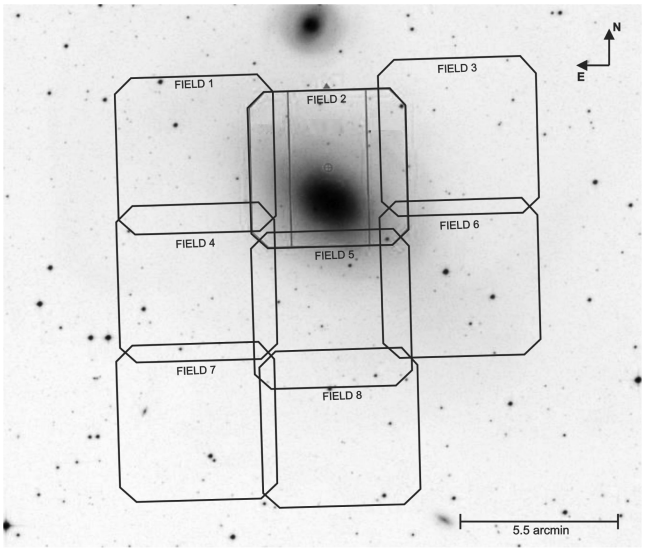

Figure 1. The positions of the eight GMOS fields superposed to the DSS image of NGC 1316.

GPREPARE, GBIAS, GIFLAT, GIREDUCE, GMOSAIC), and applying the appropriate bias and flat-field corrections. The bias and flat-field images were acquired from the Gemini Science Archive (GSA) as part of the standard GMOS baseline calibrations.

The GMOS South EEV CCDs had significant fringing in the i' filter. To subtract this pattern from our data, it was necessary to create fringe calibration images from seven blank field images downloaded from the GSA (see Table 1). These baseline calibrations, although not taken on the same dates as those for NGC 1316, were sufficiently close to allow removing the above-mentioned effect. These frames were used to correct i' images by means of the GIFRINGE and GIRMFRINGE tasks.

Finally, in order to create a final image per field, suitable for photometry, all the individual exposures of the same filter were co-added using the task IMCOADD.

2.2 Photometry

As a previous step to the photometric measures, the luminous halo of NGC 1316 was removed using a script that combines features

[1] IRAF is distributed by the National Optical Astronomical Observatories, which are operated by the Association of Universities for Research in Astronomy, Inc., under cooperative agreement with the National Science Foundation.

Table 2. Multicolour photometry for all sources detected by SExtractor in the NGC 1316 fields. Magnitudes and colours are corrected for interstellar extinction. The complete photometry is available as Supporting Information with the online version of the paper.

ID	α_{J2000} (h:m:s)	δ_{J2000} (° ′ ″)	g'_0	Errg'_0	$(g-r)'_0$	Err$(g-r)'_0$	$(r-i)'_0$	Err$(r-i)'_0$
1	3:22:40.9	−37:13:43.8	24.313	0.029	0.535	0.043	0.459	0.046
2	3:22:48.9	−37:13:43.8	24.900	0.040	0.360	0.059	0.474	0.066
3	3:22:51.6	−37:13:43.8	25.483	0.050	0.276	0.088	0.309	0.129

of SExtractor (Bertin & Arnouts 1996) and different tasks of IRAF, following the guidelines mentioned in Faifer et al. (2011). This process also generates a list of all sources detected by SExtractor.

Although all images used for the photometry showed high quality, the search for sources was conducted only on the g' images, because the signal-to-noise ratio is slightly better than in the other bands (see Section 2.4).

Point spread function (PSF) photometry was performed using DAOPHOT/IRAF routines (Stetson 1987). The PSF was determined through measurements of about two dozen of isolated and well-exposed objects located throughout the fields. In all cases, a Moffat25 model was adopted, since this model led to smaller rms than the Gaussian and Moffat15 options.

Once obtained the model that ensures the best fit, we run ALLSTAR task to get PSF magnitudes for all objects detected by SExtractor.

As a final step, we used the MKAPFILE task to derive suitable aperture correction for the PSF magnitudes.

2.3 Calibration

The NGC 1316 photometry was transformed to the standard system using the E2-A standard star field from the 'Southern Standard Stars for the u' g' r' i' z' System' of Smith (2007),[2] which was observed on the same night as the central field (which contains the galaxy). These images were reduced using the same bias and flats-fields that were applied to our science data.

The standard field includes five stars with a $(g-r)'$ colour range from 0.5 to 1.05.

The photometric zero-point calibration for all images observed under photometric conditions were derived adopting

$$m_{std} = m_{zero} + m_{inst} - K_{CP}(X-1) + A_p, \quad (1)$$

where m_{std} are the standard magnitudes, m_{zero} is the photometric zero-point, m_{inst} are instrumental magnitudes, K_{CP} is the mean atmospheric extinction at Cerro Pachón given by the Gemini web page,[3] X is the airmass and A_p is the aperture correction for the PSF magnitudes.

The analysis of the differences between the standard and instrumental magnitudes, so obtained, shows no significant trend with the colours of the standard stars in any of three g', r', i bands, i.e. colour terms are zero (to within ± 0.02 mag) in agrement with previous results by the Gemini South staff.

For the remaining seven fields, we sought for sources in common between the central field. In each overlapped region we found between 10 and 15 isolated and well-exposed objects. Once identified, we determined the offsets to bring them to standard photometric system obtained for the first one. The offsets applied were lower than 0.1 mag, except in filter g' between the fields 2 and 3, where the correction was 0.35 mag. The rms in all cases do not exceed 0.05 mag.

Subsequently, we corrected by interstellar extinction considering the value indicated by Schlafly & Finkbeiner (2011), $A_{g'} = 0.069$ mag, $A_{r'} = 0.048$ mag, $A_{i'} = 0.035$ mag, corresponding to a colour excess $E(B-V)$ =0.018.

The magnitudes and colours, corrected for interstellar extinction (denoted with the '0' subscript), for all sources detected by SExtractor in NGC 1316 are given in Table 2.

2.4 Completeness

A completeness test was carried out in order to quantify the detection limits of our photometry. Artificial stars were added to each g'-band image. They were distributed with galactocentric radius following a power law (i.e. r^{-1}), in the fields that contain the galaxy. We selected this particular law, because it represents a good approximation of the slope that follows the GCs in their spatial distribution. In cases where the galaxy halo is weak, the artificial stars were added in a uniform way. For this process we used the STARLIST and ADDSTAR tasks.

The artificial objects were separated into bins of 0.1 mag covering a range in g'_0 from 18 to 26 mag. 200 point sources were added to the original g' images in each magnitude bin. We then performed the search for sources in the same way as the original frames and thereby we got the fraction of recovered objects for each magnitude range.

As an example, Fig. 2 shows the results of the completeness tests, as a function of galactocentric radius, for different limiting magnitudes g'_0. At $g'_0 = 23.50$ our photometry is almost complete outwards a galactocentric radius $R_{gal} = 45$ arcsec while, increasing the limiting magnitude to g'_0 to 25.0, yields a completeness factor close to 90 per cent outwards $R_{gal} = 90$ arcsec.

Subsequently, the analysis was performed as a function of the colour of the artificial objects, in order to evaluate the presence of a colour bias in the completeness level. We have chosen five fixed colour values, i.e. $(g-i)'_0 = 0.0$, 0.4, 0.8, 1 and 1.2, which practically comprise the entire colour range of GC candidates (see Section 3.2). Our experiments show that for colours from 0.4 to 1.2, the behaviours of the completeness is similar to that mentioned in the previous paragraph for the whole mosaic. However in the field which contains the galaxy, we have found that our photometry has a lower completeness level for objects bluer than $(g-i)'_0$ =0.4. Specifically, for objects with $(g-i)'_0 = 0.0$, our sample is complete at 80 per cent for $R_{gal} > 90$ arcsec at $g'_0 = 24$ mag. In the same region, for objects with $g'_0 > 24$ mag, the completeness decreases for this bluest group reaching 50 per cent at $g'_0 = 25$.

2.5 Selection of unresolved sources and the $(g-i)'_0 - g'_0$ colour–magnitude diagram

At the distance of NGC 1316, we expect GC candidates to be unresolved sources. Therefore, the Stellarity index of SExtractor

[2] http://www-star.fnal.gov/Southern_ugriz/New/index.html
[3] http://www.gemini.edu/?q=node/10445

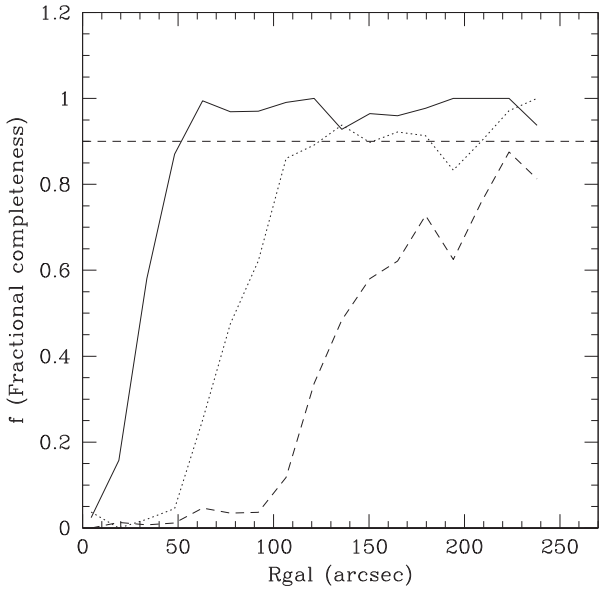

Figure 2. Completeness of the photometry as a function of the galactocentric radius for three different limiting magnitudes: $g'_0 = 23.5$ (solid line), $g'_0 = 25.0$ (dotted line) and $g'_0 = 25.8$ (dashed line). The horizontal line indicates a 90 per cent level.

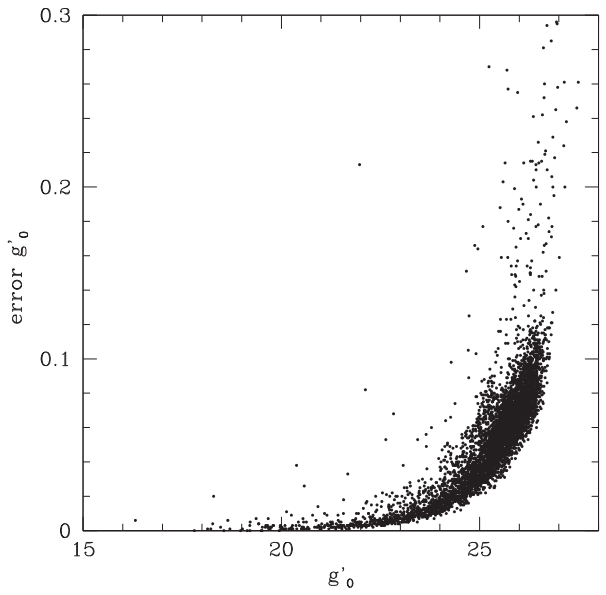

Figure 3. Photometry errors of the g'_0 magnitude for all the unresolved objects in the sample. At $g'_0 = 25.0$ the median error is $\approx \pm 0.04$ mag.

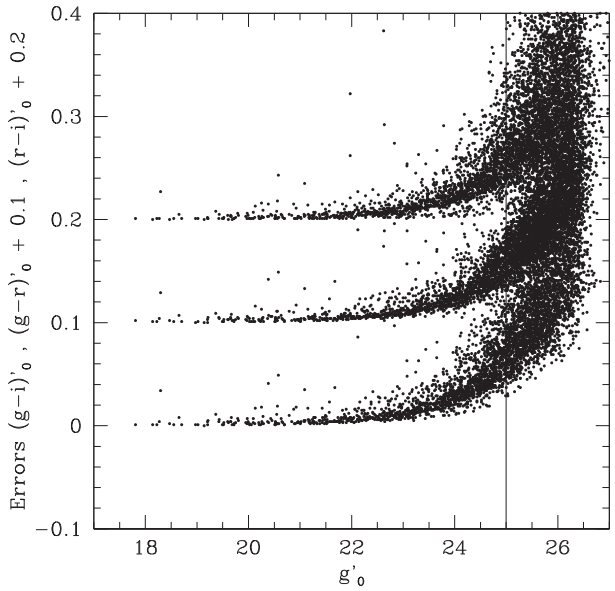

Figure 4. Photometry errors for the $(g-i)'_0$, $(g-r)'_0$ and $(r-i)'_0$ colour indices (arbitrarily shifted upwards) as a function of the g'_0 magnitude, for all the unresolved objects in the sample. The vertical line indicates the limiting magnitude of the analysis presented in this work.

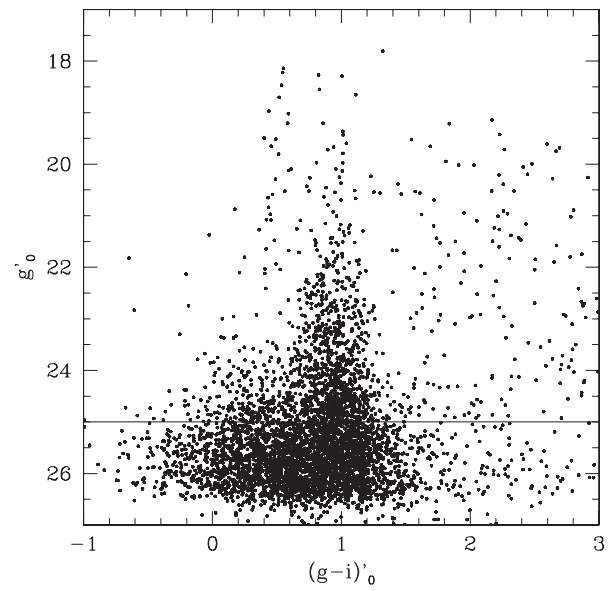

Figure 5. g'_0 versus $(g-i)'_0$ colour–magnitude diagram for the unresolved sources (4856 objects). The horizontal line at $g'_0 = 25.0$ indicates the limiting magnitude of the analysis presented in this work.

(0 for resolved objects and 1 for unresolved ones) was used to perform the object classification. We set resolved/unresolved boundary in 0.5.

In Fig. 3, we show the error on g'_0 magnitudes for all the unresolved objects in the sample. The median error at $g'_0 = 25.0$ is $\approx \pm$ 0.04 mag. In turn, the errors on the $(g-r)'_0$, $(r-i)'_0$ and $(g-i)'_0$ colours are displayed as a function of magnitude g'_0 in Fig. 4. The vertical line indicates the limiting magnitude of the analysis presented in this work, for which the median photometric errors are $\approx$ 0.06 mag. Increasing the limiting magnitude leads to rapidly increasing errors in the colours, as shown in these last figures, conspiring against the detection of eventual structures in the GCs colour distribution.

The colour–magnitude diagram, Fig. 5, corresponds to 4856 unresolved objects and exhibits some well-known features already noticed in previous works, i.e. a broad colour distribution with an extended blue tail for GC candidates fainter than g'_0=23.5. Intermediate colour objects ($(g-i)'_0 \approx 0.90$) include some GC candidates as bright as g'_0=19.0.

In particular, Goudfrooij et al. (2001b) find that an important fraction of the intermediate colour clusters is significantly brighter than their counterparts in the MW.

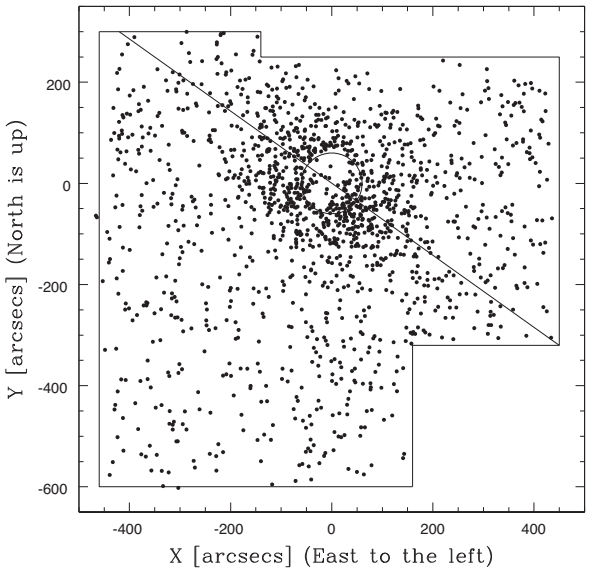

Figure 6. X and Y mosaic positions. Only 'point' sources brighter than $g'_0 = 25.0$ and $0.0 < (g-i)'_0 < 1.35$ (1280 from a total of 4856 objects) are shown. The reference circle, centred on the NGC 1316 nucleus (α_{J2000}= $3^h22^m41\overset{s}{.}7$; δ_{J2000}= $-37°12'28''$), has a 60 arcsec radius. The straight line indicates the position of the major axis of the galaxy (PA =55°).

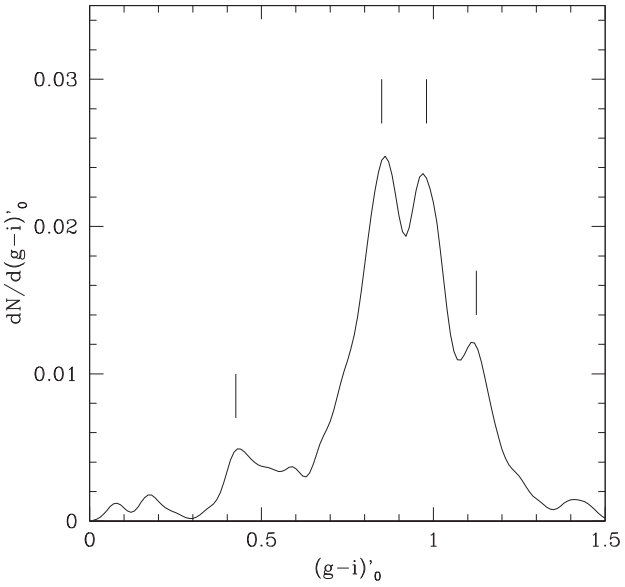

Figure 7. Smoothed $(g-i)'_0$ colour distribution for all objects in the mosaic field and brighter than $g'_0 = 23.50$. The four vertical lines at 0.42, 0.83, 0.96 and 1.13, indicate the modal colours of the four stellar cluster populations discussed in the text.

3 DISTRIBUTION ON THE SKY AND COLOUR RELATIONS FOR GC CANDIDATES

3.1 Distribution on the sky

The distribution of unresolved objects brighter than $g'_0 = 25$ (as well as the contour of the CCD mosaic) is displayed in Fig. 6. The reference circle is centred on the galaxy nucleus and has a radius of 60 arcsec. The low completeness within this region is a consequence of both the innermost dusty structure (e.g. Carlqvist 2010; Duah Asabere et al. 2014) and of the brightness of the nuclear region of the galaxy. The straight line with a PA of 55 deg, corresponds to the position of the major axis of the galaxy derived with the task ELLIPSE between galactocentric radii of 5 and 90 arcsec.

This figure shows a clear concentration around the galaxy centre and a detectable flattening of the spatial distribution of the point sources along the major axis of NGC 1316. This means that most of these sources in our sample are genuine GCs and that we are seeing the flattening already noticed by Gómez et al. (2001).

3.2 $(g-i)'_0$ colour distribution

Old GC systems in elliptical galaxies exhibit typical colour ranges $(g-r)'_0 = 0.3$–0.95, $(g-i)'_0$ 0.4–1.4 and $(r-i)'_0$ = from 0.0 to 0.6 (e.g. Harris 2009; Faifer et al. 2011; Kartha et al. 2014). In the case of NGC 1316, where the existence of a young cluster population has been reported, and as a first approach, we extend the bluest limit to $(g-i)'_0 = 0.0$.

In particular, the colour distribution of the GCs in NGC 1316 has been described as 'unimodal' although 'two colour peaks' can be detected for the brightest objects (e.g. Richtler et al. 2012b).

In addressing this issue, we first looked for a limiting magnitude g'_0 that could guarantee both low photometric errors and a low contamination level by field interlopers.

Fig. 7 displays the smoothed $(g-i)'_0$ colour distribution for objects brighter than $g'_0 = 23.5$, adopting a Gaussian kernel of 0.025 mag, comparable to the photometric error of the $(g-i)'_0$ colour. This diagram shows three well-defined peaks at 1.13, 0.96, 0.83 and a fourth, less evident one, at 0.42.

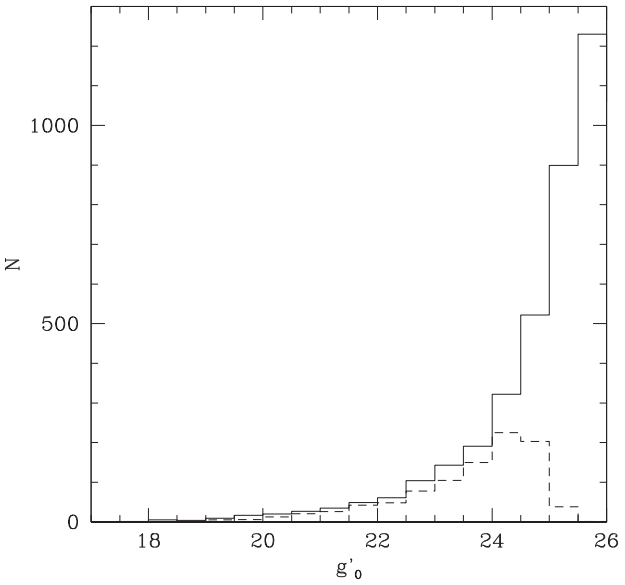

Figure 8. Comparison of the distribution of the g'_0 magnitudes presented in this work (solid lines) with that of the objects in common with Richtler et al. (2012b, dashed lines).

In what follows, we attempt to compare these colour peaks with those found by Richtler et al. (2012b) on the basis of their $(C-R)$ colours. Our photometry includes a total of 990 objects in common with those authors. The distribution of the g'_0 magnitudes for these objects is displayed in Fig. 8. This diagram shows that both samples are very similar down to $g'_0 = 24.0$. At this magnitude, our errors on the $(g-i)'_0$ colours are about half of those of the $(C-R)$ photometry. Besides, between g'_0 24 and 25, our completeness is about two times larger than that of Richtler et al.

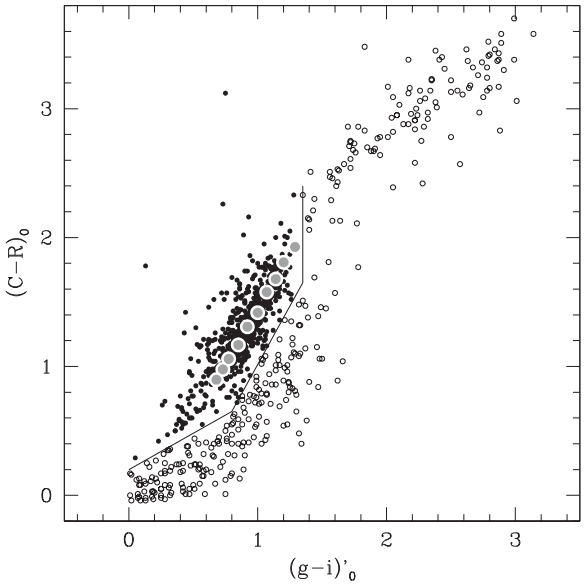

Figure 9. $(C-R)_0$ versus $(g-i)'_0$ diagram for 990 objects in common with Richtler et al. (2012b). Solid dots are GC candidates while open ones are considered as field objects. The broken line is a tentative boundary between both kind of objects. The grey dots display the $(C-T_1)_0$ versus $(g-i)'_0$ relation determined from a GCs field in NGC 4486, shifted by −0.13 mag in ordinates.

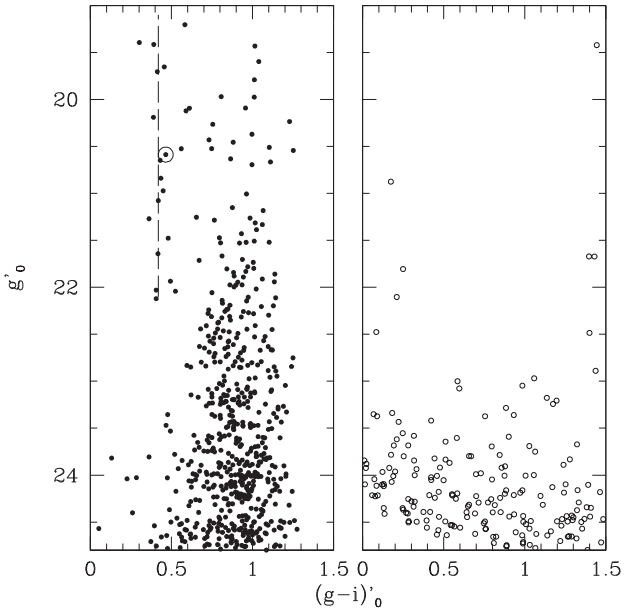

Figure 10. g'_0 versus $(g-i)'_0$ colour-magnitude diagrams for the objects shown in Fig. 9. Left: GC candidates. The circled dot is the GC candidate number 119 in Goudfrooij et al. (2001a). Right: field interlopers. The dashed line corresponds to the bluest peak in Fig. 7.

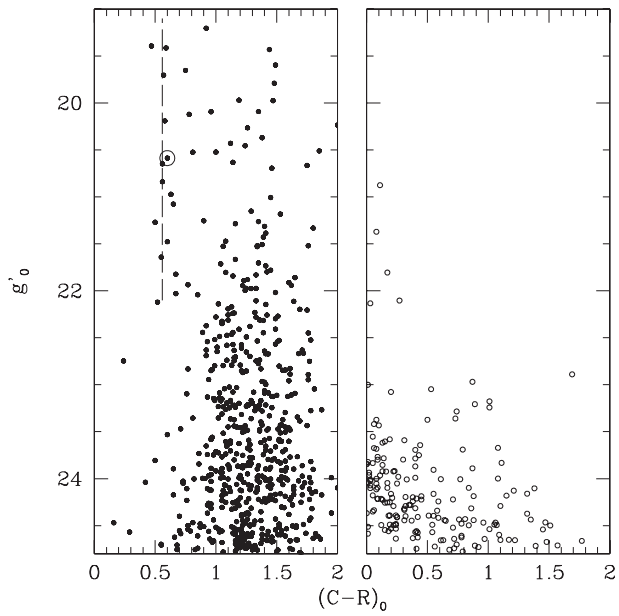

Figure 11. g'_0 versus $(C-R)_0$ colour-magnitude diagrams for the objects shown in Fig. 9. Left: GC candidates. The circled dot is the GC candidate 119 in Goudfrooij et al. (2001a). Right: field interlopers. The dashed line corresponds to the bluest peak in Fig. 7.

The relation between the $(C-R)_0$ and $(g-i)'_0$ colours is displayed in Fig. 9. This diagram also includes the $(C-T_1)_0$ versus $(g-i)'_0$ colour sequence determined by Forte et al. (2013) shifted by −0.13 mag in ordinates. Most of the 'genuine' GCs in NGC 1316 fall on this last sequence.

From this diagram, we find that the colour peaks determined by Richtler et al. at $(C-R) = 1.1$ and 1.4 correspond to those at $(g-i)'_0$ 0.83 and 0.96 in Fig. 7.

The broken line in Fig. 9 is a tentative boundary between clusters and field objects. CG candidates and field objects, so defined, have clearly distinct behaviours in the colour–magnitude diagrams displayed in Figs 10 and 11, where the g'_0 magnitudes are plotted versus $(C-R)_0$ and $(g-i)'_0$, respectively. The vertical lines centred at $(C-R)_0$=0.55 and $(g-i)'_0$ =0.43 correspond to the bluest peak shown in Fig. 7.

The last two figures include a cluster (GC 119) with confirmed membership in NGC 1316 according to its RV Goudfrooij et al. (2001a) that, as noted by Richtler et al. (2012b), could be a very young cluster.

As a first step, we analyse the global properties of the cluster system in an area defined by an outer galactocentric radius of 270 arcsec, for which we have a complete areal coverage and a completeness level that reaches ≈ 90 per cent at 45 and 90 arcsec for objects brighter than $g'_0 = 23.50$ and 25.00 mag, respectively.

The $(g-i)'_0$ colour distribution of cluster candidates brighter than $g'_0 = 23.5$ mag within annular regions defined between 45–90, 90–150 and 150–270 arcsec are displayed in Fig. 12. These distributions are normalized to the total number of clusters in the $(g-i)'_0$ colour range from 0.00 to 1.35.

This diagram shows that the two more prominent peaks in the colour distribution for objects with galactocentric radius between 90 and 150 arcsec, are 0.03 mag bluer than those at the inner and outer annuli. This feature is also observed when the limiting magnitude of the GC sample is increased to $g'_0 = 25.0$, suggesting the presence of differential reddening possibly arising in the complex structure of shells and ripples described by Schweizer (1981). In what follows, however, and being a small colour shift, we do not attempt any further correction to the $(g-i)'_0$ colours.

In turn, Fig. 13 shows the colour distribution of the whole GC sample between 45 and 270 arcsce (upper and middle panels).

From the $(C-R)_0$ and $(g-i)'_0$ diagram, we estimate that, within the colour range of the GC candidates brighter than $g'_0 = 23.50$, the contamination by field interlopers is about 5 per cent, and increases to 16 per cent when that limit is increased to g'_0 =25.0.

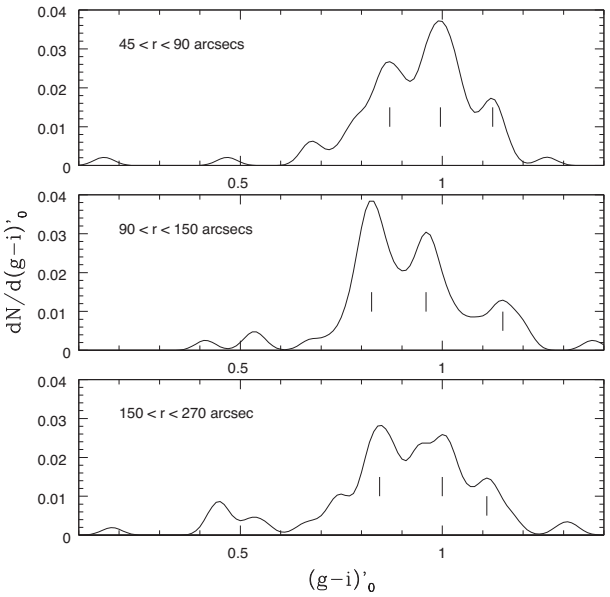

Figure 12. Smoothed $(g-i)'_0$ colour distribution for objects brighter than $g'_0 = 23.5$ and galactocentric radius ranges of 45–90 arcsec (upper panel), 90–150 and 150–270 arcsec. The vertical lines indicate the modal colour values.

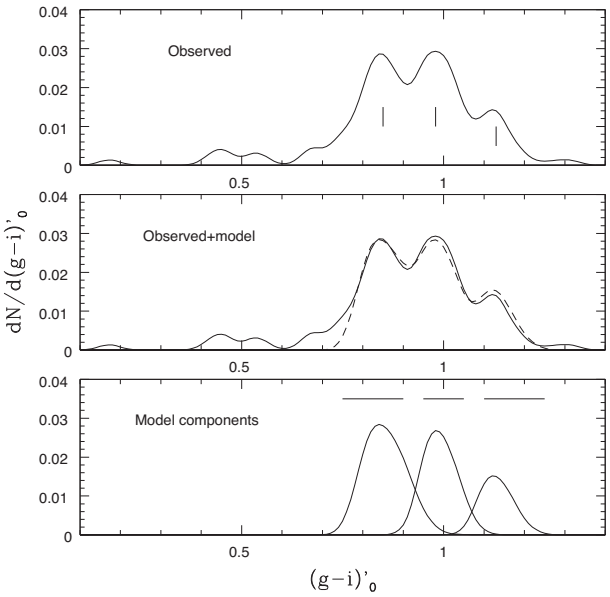

Figure 13. Normalized $(g-i)'_0$ colour distribution for all the objects included in the previous figure (upper panel). The vertical lines show the modal colours of the blue, intermediate and red GCs. The middle panel displays a comparison with the model fit described in the text. The three components of this model are shown in the lower panel.

The $(g-i)'_0$ colours of the GC candidates are displayed as function of galactocentric distance in Fig. 14. This diagram shows that the innermost regions of the galaxy exhibit a larger number of blue objects than the outer regions. This is compatible with Gómez et al. (2001), who found an 'inverse' colour gradient (i.e. GCs become bluer inwards). A common feature in elliptical galaxies is the existence of a rather constant lower blue boundary for the blue GCs while, for red GCs, the upper colour boundary becomes redder

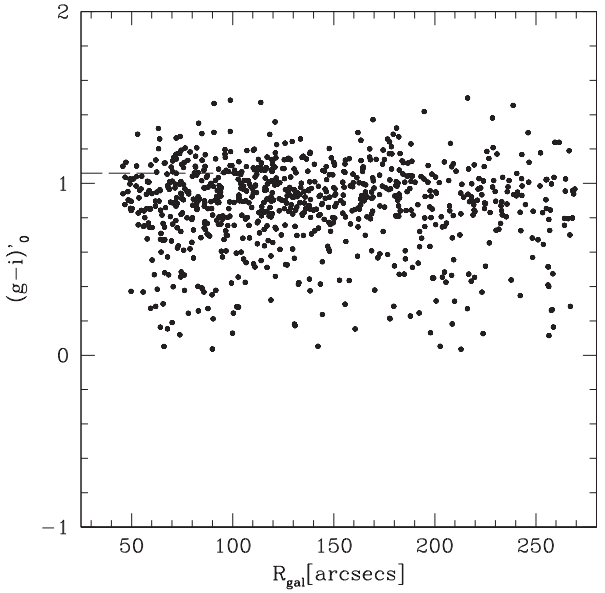

Figure 14. $(g-i)'_0$ colours as a function of galactocentric radius for GC candidates brighter than $g'_0 = 25.0$. This diagram shows that blue GC candidates are more abundant in the inner region of the galaxy. The dotted line indicates the colour of the galaxy halo within 100 arcsec in galactocentric radius (see text).

when the galactocentric decreases. This is opposite to the behaviour displayed in Fig. 14.

According to the experiments mentioned in Section 2.4 the completeness level for objects bluer than $(g-i)'_0 = 0.4$ is lower than that for redder candidates. Therefore, this 'inverse' colour gradient could be stronger than that seen in the figure.

This figure also includes the colour of the galaxy halo inside 100 arcsec, $(g-i)'_0 = 1.05$, obtained from our innermost GMOS field. Due to the uncertainty in the sky brightness, this is just an indicative value and we are not able to determine the eventual presence of a colour gradient, in fact detected by Richtler et al. (2012b) at galactocentric radii larger than 60 arcsec.

Fig. 15 displays the $(g-r)'_0$ versus $(r-i)'_0$ colours corresponding to GC candidates brighter than $g'_0 = 23.5$ and galactocentric distances from 45 to 270 arcsec. The straight lines in this diagram indicate constant $(g-i)'_0$ colours corresponding to the four colour peaks shown in Fig. 7.

In order to determine the characteristic $(g-r)'_0$ and $(r-i)'_0$ colours of each of the colour peaks, we looked for the modal colours along the (negative unit slope) straight lines, on which the r'-band colour errors correlate, within bands of 0.05 mag wide and centred at the modal $(g-i)'_0$ colours.

With this procedures we derive (0.26; 0.57), (0.33; 0.63) and (0.40; 0.73) for the $((r-i)'_0; (g-r)'_0)$ colours of the 'blue', 'intermediate' and 'red' clusters, respectively. These colours agree within $\pm$ 0.01 mag with those derived when the limiting magnitude of the sample is increased to $g'_0 = 25.0$.

In the case of the very blue clusters we show an eyeball estimate: $(g-r)'_0 = 0.32$; $(r-i)'_0 = 0.10$.

Monte Carlo simulations indicate that the typical uncertainties of the modal colours, so determined, are $\approx \pm$ 0.015 mag.

The four modal colours are shown in Fig. 16 and compared with the revised colour–colour relation determined for GC candidates in a peripheral field of NGC 4486 by Forte et al. (2013). The modal colours of the 'blue' and 'red' GC in NGC 1316 fall close to that

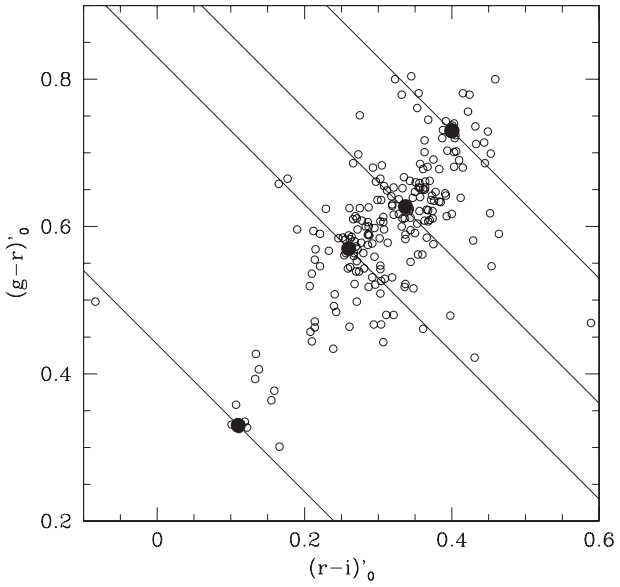

Figure 15. $(g-r)'_0$ versus $(r-i)'_0$ colours for objects brighter than $g'_0 = 23.5$ and in the galactocentric range from 45 to 270 arcsec. The lines correspond to the modal $(g-i)'_0$ colours of the 'very blue', 'blue', 'intermediate' and 'red' cluster populations.

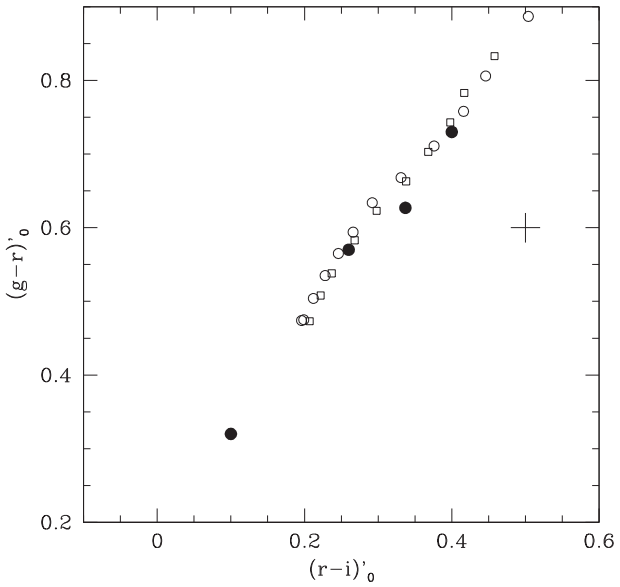

Figure 16. Modal $(g-r)'_0$ and $(r-i)'_0$ colours for the 'very blue', 'blue', 'intermediate' and 'red' cluster populations (filled dots). Open squares represent the modal colours determined for GCs in the field of NGC 4486 (M87). Open dots: PARSEC model 12 Gyr isochrone, after correcting g'_0 magnitudes (see text). The cross indicates typical errors for the observed modal colours.

relation. In turn, the 'intermediate' GCs seem shifted by −0.03 mag in $(g-r)'_0$ and +0.04 in $(r-i)'_0$.

4 COMPARISON WITH SSP MODELS

This section presents a preliminary attempt to determine the characteristic ages and chemical abundances of the stellar cluster populations on a purely photometric basis.

Table 3. Empirical colour–colour relation from GCs in NGC 4486. The chemical abundances [Z/H] are from the Usher et al. (2012) calibration.

$(g-r)'_0$	$(r-i)'_0$	[Z/H]
0.473	0.207	− 2.013
0.508	0.222	− 1.640
0.538	0.237	− 1.324
0.583	0.268	− 1.062
0.623	0.298	− 0.817
0.663	0.338	− 0.538
0.703	0.368	− 0.294
0.743	0.398	− 0.050
0.783	0.417	0.160
0.833	0.458	0.474

As well known, this kind of analysis suffers from the colour-age-chemical abundance degeneracy and any conclusion will require a validation with the results from spectroscopic work. Furthermore, these results will be strongly dependent on the adopted stellar population synthesis model.

4.1 Model selection

Several synthesis models for SSP are available in the literature and a thorough discussion of all their characteristics is beyond the scope of this paper.

However, as a first step to choose a given model, we looked for those that provide a good representation of the several colour–colour relations observed in a reference field in NGC 4486 (e.g. Forte et al. 2013). The GC sample in that field is presumably dominated by old 'bona-fide' clusters.

The colour–colour relations presented in the last paper have been improved to remove zero-point differences between different works (Forte et al., in preparation) and provide colour indices in the SDSS system. In particular, the updated $(g-r)'_0$-$(r-i)'_0$–[Z/H] relation is given in Table 3.

An overview of different SSP models shows that colour indices observed for GCs in NGC 4486, and involving the riz' bands, are fully consistent with the PARSEC models by Bressan et al. (2012) without requiring any zero-point corrections.

In turn, the PARSEC colour indices including the g'-band magnitudes, require a small correction that seems dependent on chemical abundance. In particular, we find that a correction to the model g' magnitudes:

$$\Delta g' = -0.04([\mathrm{Z/H}] + 2.2) \quad (2)$$

to the 12 Gyr model with a Salpeter initial mass function, leads the model $(g-r)'_0$–$(r-i)'_0$ relation to within ± 0.02 mag from the empirical relation in the whole colour range.

The maximum correction to the g'_0 magnitudes amounts to −0.11 mag in all range [Z/H] (from −2.2 to 0.6) and its origin is not yet clear.

The so corrected PARSEC models also show a small inflection in the $(g-r)'_0 - (r-i)'_0$ plane, as shown later, that is not a common feature with other SSP models. This relation, for a 12 Gyr model, is given in Table 4 and compared with the empirical one in Fig. 16.

Tables 3 and 4 also give the chemical abundances [Z/H] based on spectroscopic observations of the Calcium triplet lines presented by Usher et al. (2012). This 'broken line' calibration, that has a change of slope at $(g-i)'_0 = 0.77$, is in excellent agreement with

Table 4. PARSEC model colour–colour–chemical abundance relation, for an age of 12 Gyr and an assumed Salpeter initial mass function, and including a correction to g'_0 magnitudes (see text).

$(g-r)'_0$	$(r-i)'_0$	[Z/H]
0.474	0.196	−2.182
0.475	0.199	−1.881
0.504	0.212	−1.705
0.535	0.228	−1.483
0.565	0.246	−1.279
0.594	0.266	−1.006
0.634	0.292	−0.750
0.668	0.331	−0.501
0.711	0.376	−0.252
0.758	0.416	0.000
0.806	0.446	0.250
0.887	0.504	0.602

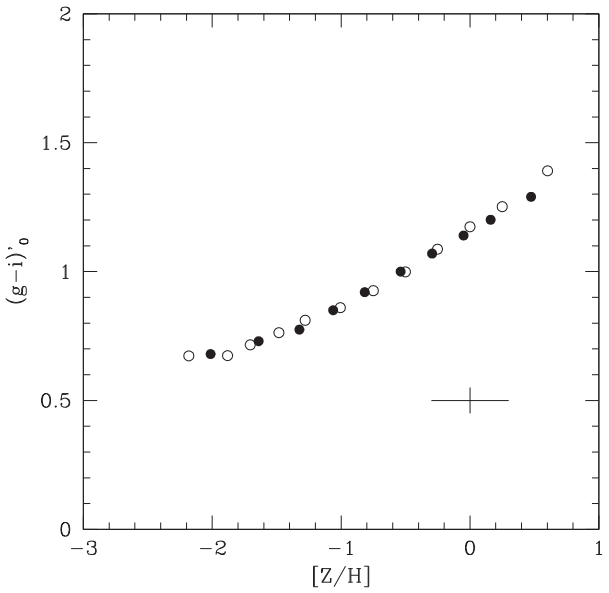

Figure 17. Chemical abundance [Z/H] versus $(g-i)'_0$ colour relation based on the Usher et al. (2012) calibration (filled dots) compared with the 12 Gyr PARSEC model including a correction to the g' magnitude described in the text. The cross shows typical errors for each data point.

the slightly curved relation predicted by the PARSEC model, as displayed in Fig. 17.

The four modal colours corresponding to the very blue, blue, intermediate and red GC populations are shown in Fig. 18 together with the PARSEC models corresponding to 1 Gyr (in the [Z/H] range from −0.25 to 0.60) and the (corrected) 5 and 12 Gyr isochrones.

4.2 Ages

Each GC population has a characteristic age that, as previously said, cannot be unambiguously determined just from photometric data. At this stage, and until spectroscopic data are not available, we make a 'reasonable' (and possibly arguable) guess about the age of each GC subpopulation.

In the case of the blue GC population, the colour peak at $(g-i)'_0 = 0.82$ is comparable to those observed in other early-type galaxies studied with the same photometric system (e.g. Kartha et al. 2014; Escudero et al. 2015). Besides, and as noticed by Goudfrooij

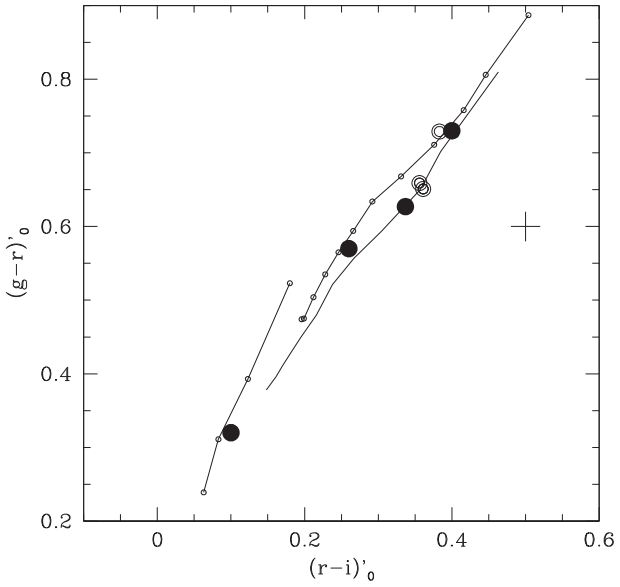

Figure 18. Corrected PARSEC model isochrone for 12 Gyr (upper line), 5 (lower line) and 1 Gyr (lower-left line). The three large solid dots towards the upper right belong to the modal colours of the 'blue', 'intermediate' and 'red' GC populations. The dot at $(r-i)'_0 = 0.10$, $(g-r)'_0 = 0.32$ is representative for the 'very blue' clusters. Double circles are confirmed GCs with spectroscopic ages and chemical abundances from Goudfrooij et al. (2001a). The cross shows typical errors of modal colours.

et al. (2001a), these clusters have photometric characteristics that are similar to those of the old blue GCs in the MW. With these arguments in mind, we adopt an age of 12 Gyr for the blue GCs in NGC 1316.

For the intermediate GCs we already noticed that their modal integrated colours, shown in Fig. 16, are offset from those of the reference field in NGC 4486 and fall on the 5 Gyr isochrone of the PARSEC models displayed in Fig. 18. This diagram also includes the only three intermediate GCs with spectroscopic age determinations, presented by Goudfrooij et al. (2001b), for which they find and age of 3 Gyr. Two of these GCs are on the PARSEC 5 Gyr isochrone.

Regarding red GCs, and as in the case of the blue GCs, we adopt a tentative age of 12 Gyr, a choice based on their brightness and colours, comparable to those observed in bright ellipticals.

The same model isochrones are shown in Figs 19 and 20 for GC candidates with galactocentric radii from 45 to 270 arcsec and larger than 270 arcsec, respectively. In these figures, the very blue cluster candidates appear close to the 1 Gyr isochrone. That isochrone displays [Z/H] values of −0.25, 0.0, 0.25 and 0.60 (blue to red) and, in particular, GC 119 appears near the colour of the very blue clusters peak and close the colours corresponding to solar metallicity. It must be stressed, however, that the model isochrone for an age of 1 Gyr is degenerate, i.e. lower metallicity models overlap in colour with those in the range displayed in Figs 19 and 20.

4.3 Chemical abundances and the modelling of the blue, intermediate and red GC populations.

An attempt to discriminate among the different GC populations on the basis of $(C-R)$ colours was presented in Richtler et al. (2012b). In our case, instead of adopting Gaussian colour distributions as these authors, we use an exponential dependence of the number of GCs as a function of Z (fractional mass chemical abundance of heavy

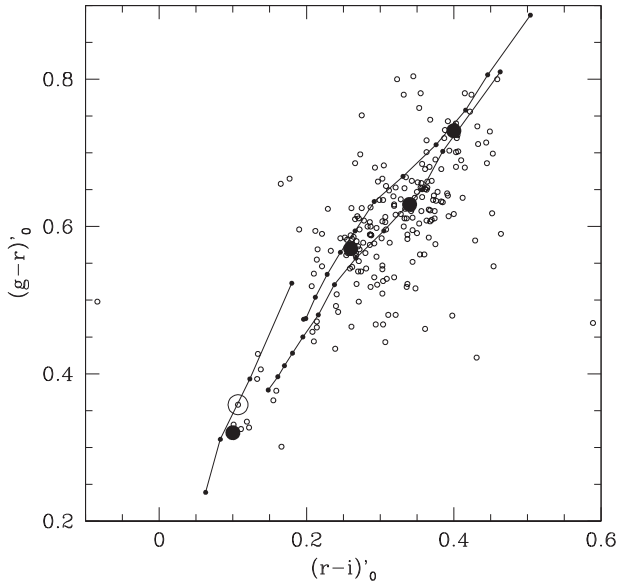

Figure 19. $(g-r)'_0$ versus $(r-i)'_0$ colours for 216 GC candidates brighter than g'_0 =23.5 and galactocentric radii between 45 and 270 arcsec. The lines correspond (left to right) to the PARSEC models for 1, 12 and 5 Gyr. The encircled dot corresponds to the cluster candidate GC 119 (see text).

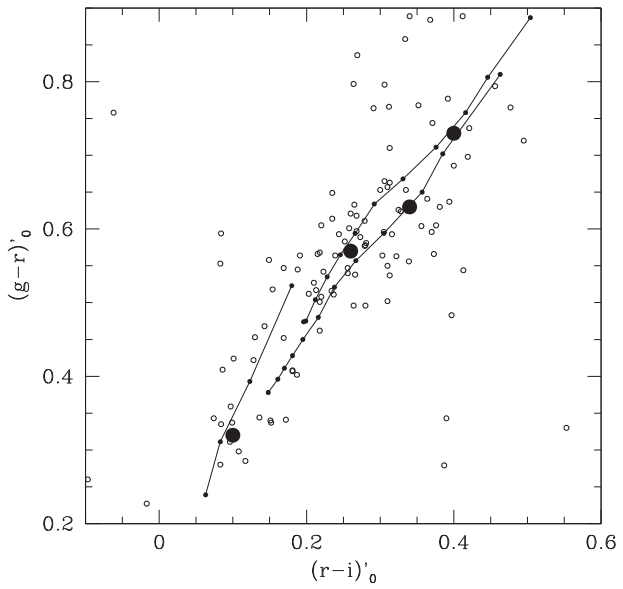

Figure 20. $(g-r)'_0$ versus $(r-i)'_0$ colours for 115 GC candidates brighter than g'_0 =23.5 and galactocentric radii larger than 270 arcsec. The lines correspond (left to right) to the PARSEC models for 1, 12 and 5 Gyr.

elements, e.g. Forte, Faifer & Geisler 2007), that we transform to $(g-i)'_0$, which is our most sensitive index to metallicity, through a given model age–metallicity relation.

The procedure is similar to that described in Forte et al. (2013) and references therein. The approach starts with a 'seed' GC chemical abundance, *Z*, obtained from a Monte Carlo generator controlled by a statistical distribution $N \approx \exp(-Z/Zs)$, within a lowest (Z_i) and maximum (Z_{max}) chemical abundances, and a scale parameter Z_s.

The $(g-i)'_0$ colour distribution of the whole cluster sample shows an extended blue tail that corresponds to presumably young clusters and field interlopers. We do not attempt to model these objects and restrict our fits to the blue, intermediate and red GCs. For

Table 5. Model fit parameters for GCs brighter than *g*=23.5 and galactocentric radii from 45 to 270 arcsec.

Pop.	*N*	Z_s	Z_i	Z_{max}	Age	Z/Z_0	[Z/H]
Blue	88	0.07	0.02	0.30	12	0.09	−1.11
Interm.	67	0.33	0.70	4	5	0.96	−0.03
Red	36	0.25	0.50	4	12	0.70	−0.16
Total	191						

Table 6. Model fit parameters for GCs brighter than *g*=25.0 and galactocentric radii from 90 to 270 arcsec.

Pop.	*N*	Z_s	Z_i	Z_{max}	Age	Z/Z_0	[Z/H]
Blue	172	0.07	0.02	0.3	12	0.08	−1.17
Interm	168	0.40	0.60	4	5	0.88	−0.06
Red	113	0.35	0.50	4	12	0.69	−0.18
Total	453						

the 'blue' GCs, we adopted $Z_i = 0.02\ Z_\odot$ and Z_{max} =0.3 $Z_\odot$ while both for the 'intermediate' and 'red' population we set Z_{max}=4 $Z_\odot$. The upper *Z* cutoff adopted for the 'blue' GCs seems appropriate for an adequate representation of the colour distributions of these clusters in a wide range of galaxy masses (e.g. Forte et al. 2014).

The $(g-i)'$ colour, determined from the colour–abundance relation, is then 'blurred' by simulating observational errors as a function of the g' magnitude. Each 'seed' GC is also characterized by an apparent g' magnitude generated adopting a Gaussian GC luminosity function with a turnover at $g' \approx 24.3$ and a dispersion $\sigma_{g'}$=1.2 mag which is comparable to the values observed in giant ellipticals (e.g. Villegas et al. 2010).

We start with a tentative initial number of objects with a given chemical abundance [*Z*/H] for each GC subpopulation, aiming at reproducing the position of the modal colours and then iterate both these numbers and the corresponding Z_s parameters until the output model gives the best match to the observed colour distribution. In this process, we ignored GC candidates bluer than $(g-i)'_0$ =0.75 that possibly belong to a the 'very blue' population.

The quality criteria of the fit is to minimize the rms of the observed versus model numbers in the colour range $(g-i)'o = 0.75$–1.35. More sophisticated approaches are probably not justified given the number of involved parameters. An assessment of the consistency of the results can be obtained by comparing the fits corresponding to two photometric samples defined through their limiting g'_0 magnitudes that we set at 23.50 and 25.0 mag.

Table 5 gives the set of parameters that provide the best representation of the 'blue', 'intermediate' and 'red' GC populations, shown in the middle and lower panels of Fig. 13 for the GC sample brighter than $g'_0 = 23.5$. In this colour–magnitude domain, the 'blue', 'intermediate' and 'red' GCs represent 87 per cent of the sample. The remaining 13 per cent are probably a combination of young clusters and 'blue' field interlopers.

Increasing the limiting magnitude to $g'_0 = 25.0$, and adopting a galactocentric range of 90–270 arcsec, leads to a GC sample 2.4 times larger. Model fit parameters for this sample are summarized in Table 6, and their colour distributions, displayed in the middle and lower panels shown in Fig. 21.

A comparison with the previous fit, shows an increase of the relative number of 'intermediate' GCs (implying a steeper integrated luminosity function for these clusters), while the chemical abundance parameters show a small change that may be explained as a

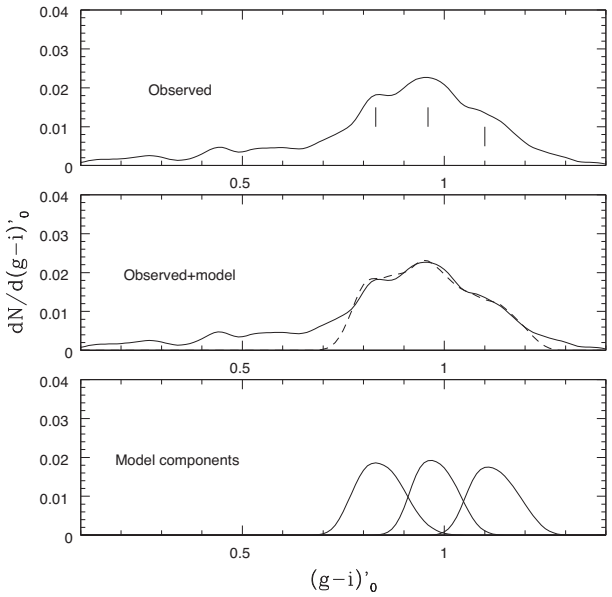

Figure 21. Normalized $(g-i)'_0$ colour distribution for objects brighter than g'_0 =25 and galactocentric radii from 90 to 270 arcsec (upper panel). This distribution is compared with a three component models (dashed lines) in the middle panel. Each of these components are shown in the lower panel.

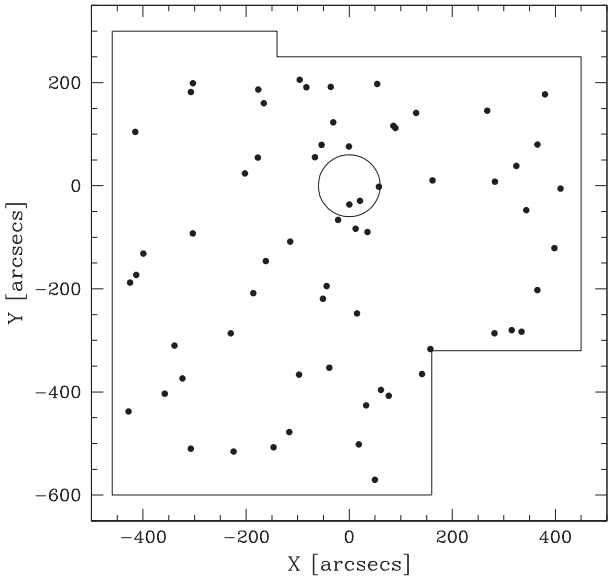

Figure 22. Distribution on the sky of 66 objects brighter than $g = 23.50$ and $(g-i)'_0$ colours between 0.30 and 0.75. The reference circle, centred on the galaxy nucleus, has a 60 arcsec radius.

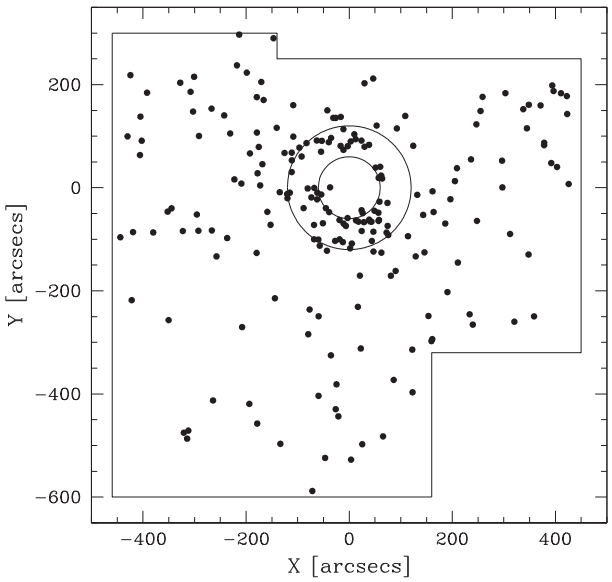

Figure 23. Distribution on the sky of 229 objects with g'_0 from 23.5 to 25 and $(g-i)'_0$ from 0.30 to 0.75. The reference circles have 60–120 arcsec radius.

consequence of an increase of the field contamination and the larger photometric errors of the fainter objects.

The [*Z*/H] abundances determined for the intermediate GCs in both model fits are slightly subsolar, a result that is in very good agreement with the spectroscopic solar abundance derived for three intermediate GCs presented by Goudfrooij et al. (2001b).

The adoption of an age of 12 Gyr in modelling the intermediate GCs would lead to much lower chemical abundances of $\approx 0.4\ Z_{\odot}$.

The age we derive for intermediate GCs is larger than that by Richtler et al. (2012b), who find an age of 2 Gyr. Part of this discrepancy might arise in the different adopted models. On the other side their $(C-R)$ colours seem −0.13 mag bluer than expected from the $(C-T_1)_0$ versus $(g-i)_0$ relation (as show in Fig. 9). A small difference between the $(C-T_1)_0$ and $(C-R)$ indices may be present (e.g. Geisler 1996), but we cannot explain the origin of the relatively large colour offset.

5 SPATIAL DISTRIBUTIONS

5.1 Distribution on the sky

In this section, we analyse the projected areal distribution of the different GC subpopulations on the sky. Previous analysis of this subject have been presented in Gómez et al. (2001), and in Richtler et al. (2012b).

In order to isolate a given GC subpopulation, and decrease the eventual contamination from the colour-adjacent populations, we define colour windows using the results of the model GC decomposition presented in previous sections. This leads to colour ranges in $(g-i)'_0$ of 0.75–0.90 for the 'blue' GCs, 0.95–1.05 for the 'intermediate' GCs and 1.05–1.35 for the 'red' GCs. The position and widths of these windows are shown in the lower panel of Fig. 13.

The distribution on the sky for 69 'very blue' objects brighter than $g'_0 = 23.5$ is depicted in Fig. 22, where these objects do not show a detectable concentration towards the centre of the galaxy. This might indicate that they are just field objects. However, as noted before, most of them appear near the 1 Gyr model isochrone in the $(g-r)'_0$ versus $(r-i)'_0$ diagram.

On the other side, there are 229 objects within the same colour range, but fainter (g'_0 from 23.5 to 25), displayed in Fig. 23. Among them, 62 appear closely packed in an annular region defined between 60 and 120 arcsec in galactocentric radius. The areal density in this annulus is some five times larger than in the rest of the mosaic field suggesting that they are associated with NGC 1316.

'Blue' GC candidates, as displayed in Fig. 24, show a concentration towards the galaxy centre and follow a rather spheroidal distribution.

In turn, intermediate GCs exhibit a marked flattening and for this population we perform an analysis of their azimuthal distribution. Azimuthal counts within a circular annulus with a complete areal

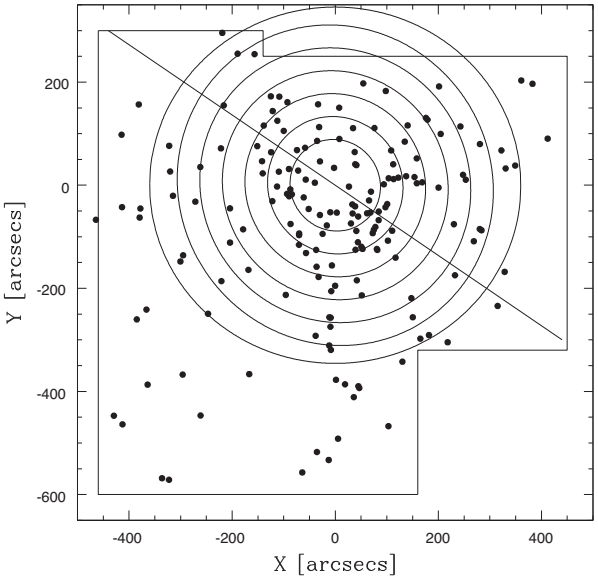

Figure 24. Distribution on the sky of 177 objects brighter than $g = 25.0$ and $(g - i)'_0$ colours between 0.75 and 0.90 ('blue' GCs). The ellipses (from a =90 to 360 arcsec) have a flattening $q = b/a = 0.96$. The straight line indicates the position of the major axis of the galaxy.

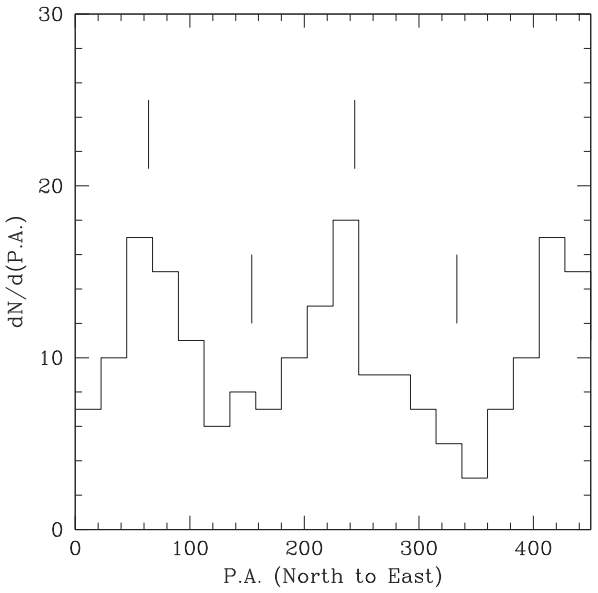

Figure 25. Azimuthal counts of 'intermediate' GC candidates in a colour window defined between $(g - i)'_0$ 0.9 and 1.05. These counts correspond to a total of 155 clusters within a circular annulus with inner and outer radii of 90 and 220 arcsec. The vertical lines show minimum and maximum values expected for an elliptical distribution with a PA of 63 deg.

coverage (inner and outer radii of 90 and 220 arcsec) are displayed in Fig. 25 where vertical lines correspond to a PA of 63 deg. This result is in excellent agreement with a previous analysis by Gómez et al. (2001).

The distribution of the intermediate GCs on the sky, as well as the elliptic annuli whose flattening and PA were determined from the azimuthal counts, are displayed in Fig. 26.

Finally, Fig. 27, corresponds to the 'red' GC candidates which exhibit a somewhat higher flattening than that corresponding to the blue GCs.

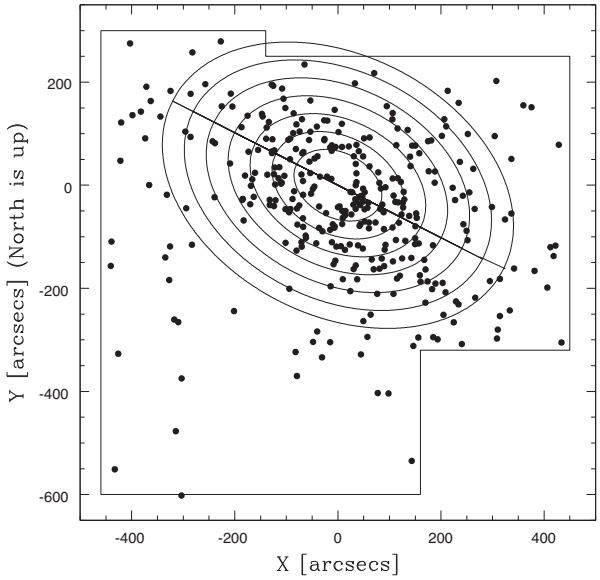

Figure 26. Distribution on the sky of 340 objects brighter than $g'_0 = 25$ and $(g - i)'_0 = 0.90$–1.05 ('intermediate' GCs). The ellipses (from a =90 to 360 arcsec) have a flattening $q = b/a = 0.70$. The ellipses have a PA of 63 deg.

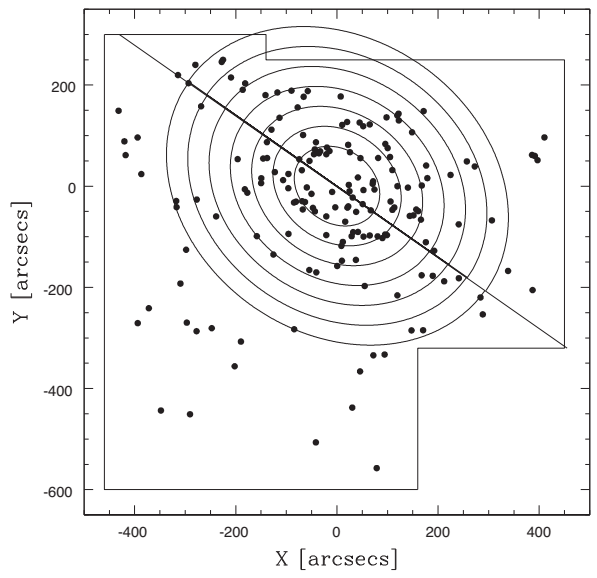

Figure 27. Distribution on the sky of 170 red GC candidates brighter than $g'_0 = 25$ and $(g - i)'_0 = 1.05$–1.35 ('red' GCs). The ellipses (from a =90 to 360 arcsec) have a flattening $q = b/a = 0.81$. The straight line indicates the position of the major axis of the galaxy.

5.2 Areal density profiles

In this subsection, we analyse the behaviour of the cluster areal distributions as a function of their corresponding semimajor axis adopting the colour windows described in the previous subsection. The areal densities correspond to a magnitude limit $g'_0 = 25.0$ and were derived in a region bounded by inner and outer semimajor axis of 90–360 arcsec. Areal incompleteness of the outermost elliptical annuli (seen in Figs 24, 26 and 27) was taken into account when computing the projected densities.

As we do not have a suitable field to estimate the level of the background contamination, we define a reference area including all

Table 7. Projected density as a function of semimajor axis for the 115 'blue' GCs with $(g-i)'_0$ =0.75 to 0.90 mag (q = 0.96, background=0.20 objects arcmin^{-2}).

Scaling law	Slope	Zero-point	rms
Power	− 2.132(0.156)	5.203(0.025)	0.062
$a^{1/4}$	− 0.986(0.083)	4.022(0.029)	0.083
Disc	− 0.0044(0.0006)	1.246(0.045)	0.111

Table 8. Projected areal density fits for 210 'intermediate' GCs with $(g-i)'_0$ =0.95–1.05 mag (q =0.70; background=0.12 objects arcmin^{-2}).

Scaling law	Slope	Zero-point	rms
Power	− 1.924(0.224)	4.75(0.036)	0.088
$a^{1/4}$	− 0.892(0.094)	3.694(0.033)	0.080
Disc	− 0.0040(0.0004)	1.188(0.030)	0.074

Table 9. Projected areal density fits for 98 'red' GCs with $(g-i)'_0$ =1.05–1.35 mag (q =0.81; background=0.08 objects arcmin^{-2}.)

Scaling law	Slope	Zero-point	rms
Power	− 2.328(0.417)	5.409(0.066)	0.164
$a^{1/4}$	− 1.082(0.189)	4.140(0.066)	0.161
Disc	− 0.0049(0.0009)	1.107(0.067)	0.166

objects with ordinates smaller than $y = -300$ arcsec in Fig. 6. This region spans 50 arcmin^2. We then derive three density profiles for the different cluster populations. Each of these profiles assumes, respectively, null contamination (i.e. there are no background contamination; open dots); a 'reference' background level assuming that half of the objects in the that area are field interlopers (filled dots), and finally, that all of the objects in the reference area are field objects (open squares). The resulting profiles then give an idea about the uncertainty connected with the adopted contamination density.

As discussed before, the very blue clusters exhibit a very sparse distribution (except the concentration detectable in the central regions of the galaxy) and we do not attempt the determination of a density profile for these objects.

Figs 24, 26 and 27 indicate that the blue, intermediate and red GC subpopulations have distinct spatial distributions and flattenings. An estimate of these flattenings was obtained by computing the ratio of the second-order momentums of the y and x coordinates defined in a rotating frame centred on the galaxy nucleus. For this estimation, only objects within a circular annulus with a complete areal coverage were considered (inner and outer radii of 90 and 220 arcsec).

In the case of the blue and red GCs, with low flattenings, the resulting PA seem consistent with that of the major axis of the galaxy (PA = 55 deg). In contrast, the intermediate GCs (as discussed before) exhibit a PA 8 deg larger than that.

Different scale laws have been adopted in the literature for the discussion of the GC density profiles. For example, power laws, de-Vaucouleurs like dependences (i.e. $r^{1/4}$) or Sérsic profiles, a particular case of which ($n = 1$) corresponds to disc-like structures.

In our approach, we performed least-squares fit adopting all these scaling laws for each of the GC subpopulations in an attempt to asses which one provides the best profile representation.

The *lsq* fits given in Tables 7–9 correspond to adopting the 'reference background' and are shown in Figs 28–30. In these diagrams,

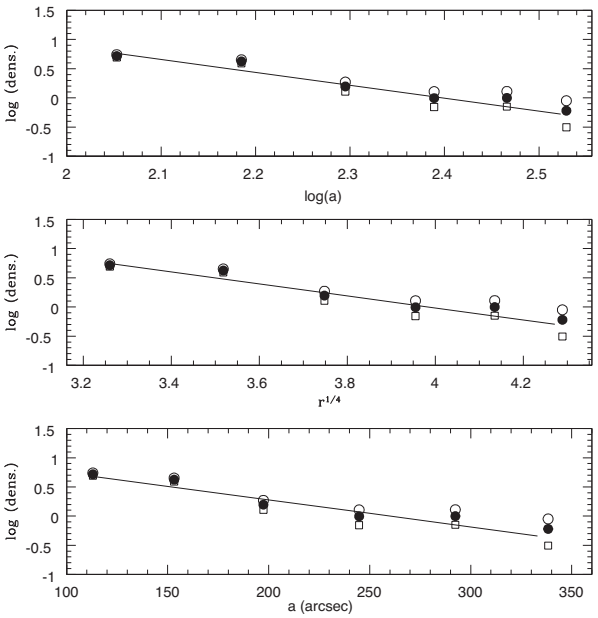

Figure 28. Projected density as a function of semimajor axis for the 'blue' clusters ($(g-i)'_0 = 0.75$–0.90 mag). A power law (upper diagram), $r^{1/4}$(middle), and disc-like (lower) profile fits are displayed.

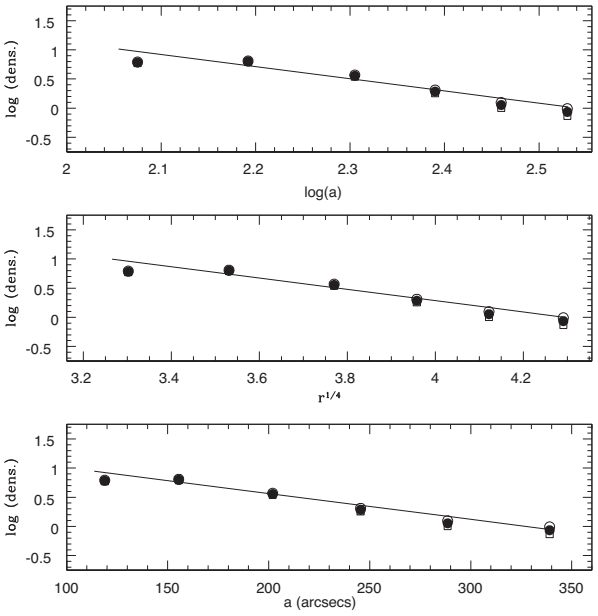

Figure 29. Areal density distribution for the 'intermediate' clusters ($(g-i)'_0 = 0.95$–1.05 mag). A power law (upper diagram), $r^{1/4}$ (middle) and disc-like (lower) profile fits are displayed.

the open and filled circles, and the open squares belong to the three background level options described before.

The uncertainties of the cluster counts within each annulus are comparable to the size of the plotting symbols.

Tables 7 and 8 show that, in terms of the rms of the fits, a power law gives the best representation of the areal density behaviour for the 'blue' clusters, while 'intermediate' GCs are better represented by a disc ($n = 1$). These two populations (despite their different flattenings and semimajor axis PA) exhibit rather similar slopes along their respective semimajor axis a.

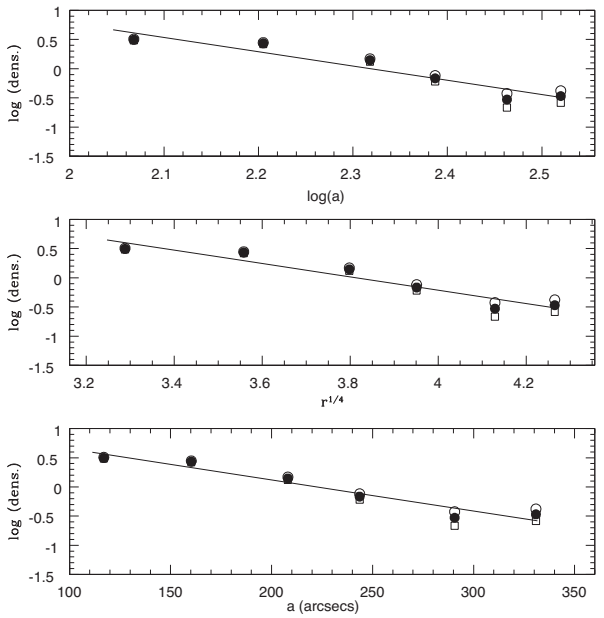

Figure 30. Areal density distribution for the 'red' clusters ($(g-i)'_0 = 1.10$–1.35 mag). A power law (upper diagram), $r^{1/4}$ (middle) and disc-like (lower) profile fits are displayed.

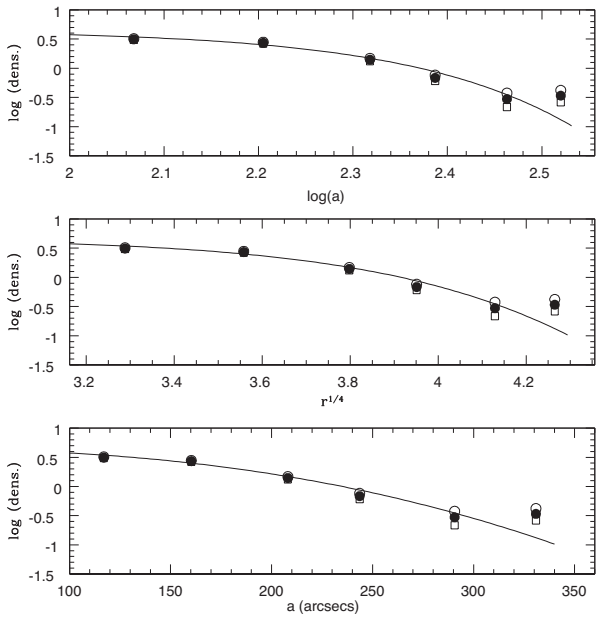

Figure 31. Areal density distribution for the 'red' clusters($(g-i)'_0 = 1.10$–1.35 mag). A Sérsic profile with a scalelength of 200 arcsec and $n = 0.4$ (see text) is shown as solid lines.

In the case of the 'red' GCs, and as shown in Table 9, none of the scaling laws seem to provide an acceptable representation since the fits leave large and systematic residuals. For these clusters, and as an alternative, we show a Sérsic profile, with an index n =0.4 and a scale parameter of 200 arcsec, that provides a better representation of the density profile, as depicted in Fig. 31.

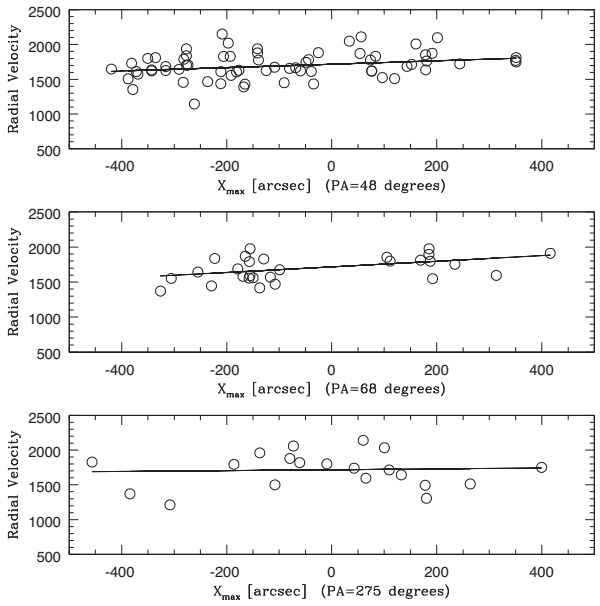

Figure 32. RVs from Richtler et al. (2014) as a function of the axis that exhibits the maximum velocity gradient for 67 blue GCs (upper panel), 28 GCs intermediate (middle panel) and 20 red GCs (lower panel). $X_{\rm max}$ =0 indicates the centre of the galaxy. The typical RV errors (∼50 km s^{-1}) are smaller than the size of the plotting symbols.

Table 10. Maximum RV gradients for the blue, intermediate and red GC populations.

Pop.	$N_{\rm GCs}$	Slope(Err)	PA (deg)	residual rms km s^{-1}
Blue	67	0.22(± 0.11)	48	195
Interm.	28	0.42(± 0.08)	68	154
Red	20	0.06(± 0.28)	275	260

6 RADIAL VELOCITIES

A revision of our photometry shows that 124 objects have RVs measured by Richtler et al. (2014). Among them, 115 fall within the colour windows we adopted to isolate the blue (67 objects), intermediate (28 objects) and red GC candidates (20 objects). The nine objects excluded are slightly bluer than the window we use to define the blue GCs, but in any case, their inclusion in the figure of the blue CG has no effect on the analysis.

For each of these groups, we found the PA on the sky of the axis that maximizes the RV gradients ($X_{\rm max}$), as shown in Fig. 32. The PA is measured from north towards east until reaching the section of the axis that contains the objects with receding RVs (i.e. velocities larger than the GC mean RV).

The parameters of these gradients are listed in Table 10 for each GC subpopulation. This table indicates that both the blue and intermediate GCs exhibit significant and different RV gradients while red GCs do not show a detectable gradient and display the largest rms of the velocity residuals.

Richtler et al. (2014), noticed that the kinematic axis of the stellar halo in NGC 1316, PA = 71 deg, is misaligned with the optical axis of the galaxy. Besides, McNeil-Moylan et al. (2012) also detect such a deviation, on the basis of the analysis of the RVs of 490 planetary nebulae, and find PA =64 deg.

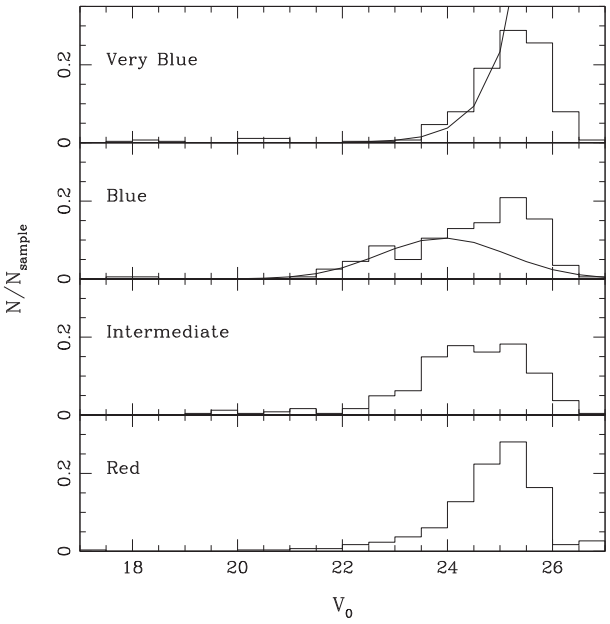

Figure 33. Integrated luminosity function for the 'very blue' clusters (upper panel), 'blue', 'intermediate', and 'red' (lower panel) GCs. As a reference, a Gaussian with a turnover at $V_0 = 23.93$ and dispersion $\sigma = 1.2$ mag, is plotted for the 'blue' globulars. An exponential is shown for the very blue objects.

The PA of the maximum RV gradient of the intermediate GCs, falls between those last angles and suggests that, at least these clusters, have a kinematic link with field stars.

7 GC LUMINOSITY FUNCTIONS

A thorough discussion of the characteristics of the integrated luminosity function of the cluster candidates requires a deep comparison field which we do not have. However, and adopting the same colour 'windows' defined in Section 5, we present a first analysis of the apparent magnitude distribution of the four cluster subpopulations that is meaningful for objects brighter than g'_0=25 and with galactocentric radius range of 90–270 arcsec, for which our completeness level is close to 90 per cent.

With the aim of comparing this analysis with previous work, we transformed the GC g'_0 magnitudes to V_0 magnitudes through the relation given by Chonis & Gaskell (2008): $V = g' - 0.011–0.587 \times (g - r)'$.

The resulting luminosity functions, uncorrected for completeness and normalized by total number of each population ($N_{\rm sample}$), are displayed in the four panels of Fig. 33 (top to bottom: 'very blue', 'blue', 'intermediate' and 'red' clusters).

The 'very blue' objects show a steep exponential behaviour, starting at $V \approx 22.0$ and with a scale parameter of 0.55 mag.

'Blue' GCs seem well represented by a reference Gaussian curve with a turnover at $V_0 = 23.93$ which we estimate adopting the distance modulus given by Cantiello et al. (2013) and assuming M_V(TO) $= -7.66$ (Di Criscienzo et al. 2006, obtained from the low-metallicity halo clusters in the MW and M31), and a dispersion $\sigma = 1.2$, typical for GCs in giant ellipticals.

The increase in the number of objects above the Gaussian, for objects fainter than $V_0 = 24$ is possibly explained by the presence of field interlopers (see Fig. 10).

The luminosity function of the 'intermediate' GCs is significantly broader than those of the remaining GC families and shows a significant fraction of GC candidates brighter than $V_0 = 22$, reaching ≈ 19 which, as discussed by Goudfrooij et al. (2001b), would be compatible with an age younger than that of the 'blue' GCs. For this population Gómez et al. (2001) determine a turnover magnitude V=24.82.

Finally, 'red' GCs, also display a rapid increase in number. This behaviour of the red GCs was previously noticed by Goudfrooij et al. (2004). The presence of a hypothetical turnover some 0.5 mag fainter than that of the 'blue' GCs that could be justified by metallicity effects (Ashman, Conti & Zepf 1995), cannot be ruled out.

8 CONCLUSIONS

The discussion of the *gri*′ photometry of cluster candidates in NGC 1316 presented in this paper, confirms earlier results that pointed out the complexity of the cluster system in this galaxy.

We identify four cluster subpopulations with distinct characteristics, namely:

(a) *Very blue clusters.* These cluster candidates occupy a $(g - i)'_0$ colour range from 0.30 to 0.75. On one side, objects brighter than g'_0 =23.5, show a very sparse distribution. Most of them show a colour distribution compatible with a 1 Gyr isochrone. Given the lack of unicity in the colour–abundance relation for that age, the situation remains largely undetermined and requires a spectroscopic analysis to clarify the nature of these objects.

GC number 119 in Goudfrooij et al. (2001b), falls in that colour range and is a confirmed member of the NGC 1316 system, on the basis of its RV. This cluster has been identified by Richtler et al. (2012b) as a presumably very young cluster.

These bright cluster candidates are an intriguing subpopulation that, if confirmed as such, would indicate the existence of an intense burst of cluster formation widespread on the whole body of the galaxy.

In turn, fainter candidates within the same colour range, show a marked increase of the areal density in an annular region (60–120 arcsec) around the centre of the galaxy. The relatively large errors of the photometry for these faint clusters, prevent a significant analysis of their position in the two colour diagram. Their exponential luminosity function suggests that they might rather be massive young clusters than GCs.

(b) *Blue GCs.* This subpopulation exhibits a colour peak at $(g - i)'_0$=0.82, similar to those observed for the blue GCs in elliptical galaxies. As noticed by Goudfrooij et al. (2001b) their photometric features are compatible with the old low-metallicity GCs in the MW halo.

(c) *Intermediate GCs.* The colours of these clusters correspond to a 5 Gyr old population in the frame of the Bressan et al. models. This age, and the mean chemical abundance we derive for these clusters (slightly subsolar), are comparable with the spectroscopic age (3 ± 1 Gyr) and abundance (solar) obtained by Goudfrooij (2012) for three GCs which, according to their colours, belong to this population.

The spatial distribution of the intermediate GCs exhibits a flattening $q \approx 0.7$ and a PA of 63 deg, i.e. some 8 deg larger than that of the semimajor axis of the NGC 1316 halo. Gómez et al. (2001) find the same PA for what they call 'red' GCs. Their areal density profile can be fit by Sérsic profile with $n = 1$ (disc like).

An analysis of the RVs of 28 intermediate GCs (with data from Richtler et al. 2014) shows marked similitude with the kinematics

of the stellar halo of the galaxy. This result argues in favour of a connection between the intermediate GCs and field stars. The presence of an intermediate age stellar population was pointed out by Cantiello et al. (2013) through a comparison of their SBF colours and SSP model colours.

(d) *Red GCs.* The colours of this population are compatible with those of old red GCs in elliptical galaxies. Their spatial distribution, spheroidal and slightly flattened, is coherent with a bulge-like high chemical abundance population (somewhat less than that of the intermediate GCs). They seem clearly distinct from the intermediate clusters. If the red GCs were coeval with the intermediate clusters, their chemical abundance should be three to four times larger than those we find on the basis of the model fits, not a very likely situation.

A summary of all these features then indicates the existence of a rather spherical low-metallicity halo, and of a more chemically enriched and flattened bulge, coexisting with an 'intermediate age' flattened spheroid (or even a thick disc?) which exhibits photometric and kinematic similarities with the galaxy halo. This scenario is compatible with McNeil-Moylan et al. (2012), who suggest that NGC 1316 may represent the early stages of a system that would evolve to become a 'Sombrero' like galaxy (NGC 4594) through a series of mergers. The so-called 'very blue' clusters, for which we find a tentative age of 1 Gyr, may be the tracers of the last of these events.

ACKNOWLEDGEMENTS

This work was funded with grants from Consejo Nacional de Investigaciones Cientificas y Tecnicas de la Republica Argentina, and Universidad Nacional de La Plata (Argentina). Based on observations obtained at the Gemini Observatory, which is operated by the Association of Universities for Research in Astronomy, Inc., under a cooperative agreement with the NSF on behalf of the Gemini partnership: the National Science Foundation (USA), the National Research Council (Canada), CONICYT (Chile), the Australian Research Council (Australia), Ministério da Ciência, Tecnologia e Inovação (Brazil) and Ministerio de Ciencia, Tecnología e Innovación Productiva (Argentina). The Gemini program ID are GS-2008B-Q-54 and GS-2009B-Q-65. This research has made use of the NED, which is operated by the Jet Propulsion Laboratory, Caltech, under contract with the National Aeronautics and Space Administration.

We thank the referee for her/his significant contributions which greatly improved this work.

REFERENCES

Ashman K. M., Conti A., Zepf S. E., 1995, AJ, 110, 1164
Bertin E., Arnouts S., 1996, A&AS, 117, 393
Bressan A., Marigo P., Girardi L., Salasnich B., Dal Cero C., Rubele S., Nanni A., 2012, MNRAS, 427, 127
Brodie J. P. et al., 2014, ApJ, 796, 52
Cantiello M. et al., 2013, A&A, 552, A106
Carlqvist P., 2010, Ap&SS, 327, 267
Carretta E., 2015, ApJ, 810, 148
Chonis T. S., Gaskell C. M., 2008, AJ, 135, 264
Di Criscienzo M., Caputo F., Marconi M., Musella I., 2006, MNRAS, 365, 1357
Duah Asabere B., Horellou C., Winkler H., Jarrett T., Leeuw L., 2014, preprint (arXiv:1409.2474)
Eggen O. J., Lynden-Bell D., Sandage A. R., 1962, ApJ, 136, 748
Escudero C. G., Faifer F. R., Bassino L. P., Calderón J. P., Caso J. P., 2015, MNRAS, 449, 612
Faifer F. R. et al., 2011, MNRAS, 416, 155
Forbes D. A., Romanowsky A. J., Pastorello N., Foster C., Brodie J. P., Strader J., Usher C., Pota V., 2016, MNRAS, 457, 1242
Forte J. C., Faifer F., Geisler D., 2007, MNRAS, 382, 1947
Forte J. C., Faifer F. R., Vega E. I., Bassino L. P., Smith Castelli A. V., Cellone S. A., Geisler D., 2013, MNRAS, 431, 1405
Forte J. C., Vega E. I., Faifer F. R., Smith Castelli A. V., Escudero C., González N. M., Sesto L., 2014, MNRAS, 441, 1391
Fukugita M., Ichikawa T., Gunn J., 1996, AJ, 111, 1798
Geisler D., 1996, AJ, 111, 480
Gómez M., Richtler T., Infante L., Drenkhahn G., 2001, A&A, 371, 875
Goudfrooij P., 2012, ApJ, 750, 140
Goudfrooij P., Mack J., Kissler-Patig M., Meylan G., Minniti D., 2001a, MNRAS, 322, 643
Goudfrooij P., Alonso M. V., Maraston C., Minniti D., 2001b, MNRAS, 328, 237
Goudfrooij P., Gilmore D., Whitmore B. C., Schweizer F., 2004, ApJ, 613, L121
Harris W. E., 2009, ApJ, 703, 939
Harris W. E., Harris G. L., Hudson M. J., 2015, ApJ, 806, 36
Kartha S. S., Forbes D. A., Spitler L. R., Romanowsky A. J., Arnold J. A., Brodie J. P., 2014, MNRAS, 437, 273
Kruijssen J. M. D., 2015, MNRAS, 454, 1658
Kruijssen J. M. D., 2016, in Meiron Y., Li S., Liu F.-K., Spurzem R., eds, Proc. IAU Symp. 312, Star Clusters and Black Holes in Galaxies across Cosmic Time. Cambridge Univ. Press, Cambridge, p. 147
McNeil-Moylan E. K., Freeman K. C., Arnaboldi M., Gerhard O. E., 2012, A&A, 539, A11
Richtler T., Kumar B., Bassino L. P., Dirsch B., Romanowsky A. J., 2012a, A&A, 543, L7
Richtler T., Bassino L. P., Dirsch B., Kumar B., 2012b, A&A, 543, A131
Richtler T., Hilker M., Kumar B., Bassino L. P., Gómez M., Dirsch B., 2014, A&A, 569, A41
Schlafly E. F., Finkbeiner D. P., 2011, ApJ, 737, 103
Schweizer F., 1980, ApJ, 237, 303
Schweizer F., 1981, ApJ, 246, 722
Stetson P. B., 1987, PASP, 99, 191
Usher C. et al., 2012, MNRAS, 426, 1475
Villegas D. et al., 2010, ApJ, 717, 603

SUPPORTING INFORMATION

Additional Supporting Information may be found in the online version of this article:

Table 2. Multicolour photometry for all sources detected by SExtractor in the NGC 1316 fields. Magnitudes and colours are corrected for interstellar extinction.
(http://www.mnras.oxfordjournals.org/lookup/suppl/doi:10.1093/mnras/stw1627/-/DC1).

Please note: Oxford University Press is not responsible for the content or functionality of any supporting materials supplied by the authors. Any queries (other than missing material) should be directed to the corresponding author for the article.

This paper has been typeset from a TEX/LATEX file prepared by the author.